Perovskite oxide ultrathin nanosheets/g-C$_3$N$_4$ 2D-2D heterojunction photocatalysts with significantly enhanced photocatalytic activity towards the photodegradation of tetracycline

Deli Jiang[a], Tianyong Wang[a], Qing Xu[a], Di Li[b], Suci Meng[a], Min Chen[a,*]

[a] *School of Chemistry and Chemical Engineering, Jiangsu University, Zhenjiang 212013, China*
[b] *Institute for Energy Research, Jiangsu University, Zhenjiang 212013, China*

ARTICLE INFO

ABSTRACT

Novel visible-light-driven 2D-2D heterojunction photocatalysts was constructed based on 2D g-C$_3$N$_4$ and exfoliated ultrathin K$^+$Ca$_2$Nb$_3$O$_{10}^-$ nanosheets, which is derived from Dion-Jacobson phase layer perovskites. The photocatalytic performance of the 2D-2D g-C$_3$N$_4$/K$^+$Ca$_2$Nb$_3$O$_{10}^-$ nanosheet heterojunctions was evaluated by the degradation of tetracycline hydrochloride under visible light irradiation. Compared with bare K$^+$Ca$_2$Nb$_3$O$_{10}^-$ and g-C$_3$N$_4$, the g-C$_3$N$_4$/K$^+$Ca$_2$Nb$_3$O$_{10}^-$ nanosheet heterojunctions exhibited considerably enhanced photocatalytic activity towards the degradation of tetracycline hydrochloride, which is about 6.6 and 1.8 times higher than that of pure K$^+$Ca$_2$Nb$_3$O$_{10}^-$ and g-C$_3$N$_4$, respectively. This enhanced activity can be mainly attributed to the synergistic effect of g-C$_3$N$_4$/K$^+$Ca$_2$Nb$_3$O$_{10}^-$ nanosheet heterojunctions with strong interfacial interaction and abundant 2D coupling interfaces, which could efficiently promote the photo-induced charge separation. The results of work demonstrated that construction of 2D-2D heterojunctions is an effective strategy to obtain the enhanced photocatalytic activity towards the degradation of tetracycline hydrochloride.

© 2016 Published by Elsevier B.V.

1. Introduction

With the development of industry and population, energy crisis and environmental pollution have directly influenced our lives. It is widely accepted that photocatalysts are significant materials for achieving a future sustainable society with graceful environment [1]. However, developing stable photocatalyst materials that can efficiently utilize solar energy for practical application is of great technical challenge [2]. In the past few years, two-dimensional (2D) nanosheets have sparked widespread interests due to their large surface-to-volume ratio [3–5], unique optical and electronic properties [6], as well as the promising applications in water splitting, solar cells and environmental purification [7]. Among various 2D nanosheets, metal oxide nanosheets that consist of Ti^{4+} or Nb^{5+} have attracted considerable attention owing to virtually infinite varieties of layered oxide materials with interesting functional properties, such as superconductors, high-κ ferroelectricity, magnetic materials and photocatalysts [8–16]. One prominent class of the metal oxide nanosheets is the ones

originated from the Dion-Jacobson phases of layered perovskites, with the prototypic member KCa$_2$Nb$_3$O$_{10}$ [17]. The nanosheets have been produced from the layered perovskite (e.g., KCa$_2$Nb$_3$O$_{10}$) via protonation, exfoliation and flocculation to form Ca$_2$Nb$_3$O$_{10}^-$ [18]. Osterloh et al. revealed photocatalytic activity of individual Ca$_2$Nb$_3$O$_{10}^-$ nanosheets for H$_2$ evolution [19]. Ebina and co-workers have demonstrated that the photocatalytic H$_2$ evolution activity of aggregated HCa$_2$Nb$_3$O$_{10}$ nanosheets from an aqueous methanol solution and overall water splitting under ultraviolet light irradiation [20]. An important aspect is that these Ca$_2$Nb$_3$O$_{10}^-$ nanosheets, consisting of perovskite building blocks of NbO$_6$ octahedra [21], are especially attractive because of their large surface area, excellent chemical stability low cost and low toxicity [22,23]. These properties make perovskite nanosheets potentially suitable for conversion of solar energy to electricity or chemical energy. However, the practical application of the perovskite nanosheets is still hindered by its main disadvantages, such as the wide band gap (about 3.4 eV) and high recombination rate of photogenerated electron-hole pairs [24,25]. Therefore, improving visible light response and prolonging the life time of charge carriers becomes a very prominent strategy for perovskite nanosheets to achieve high activity in photocatalytic application.

To address the problems, many attempts have been made to increase the photocatalytic performance of the perovskite nanosheets, such as metal doping [15,26], dye-sensitized [27], metal intercalation [28,29] and coupling with other semiconductors [30]. Construction of heterostructure photocatalysts with efficient light harvesting and fast charge transfer has attracted particular interests [31]. Especially, owing to the significant advantages of the large contact surface and the enhanced charge transfer rate in photocatalytic systems, 2D-2D heterostructures are more expected as compared with the 0D-2D and 1D-2D heterostructures [32]. Heretofore, a number of perovskite nanosheets based on 2D-2D heterostructures have demonstrated enhanced photoelectrochemical performance [33–35]. However, construction of novel 2D-2D heterojunctions with high-performance photocatalytic activities is still a challenging task.

Among various 2D nanosheets, graphitic carbon nitride (g-C_3N_4) nanosheet is especially attractive in the field of visible-light photocatalytic water splitting, CO_2 reduction, and organic syntheses [36–41], owing to its excellent properties including visible light response (band gap of 2.7 eV), extraordinary chemical stability, easy preparation and metal-free composition [42–45]. Coupling g-C_3N_4 nanosheets with wide-band-gap semiconductors to construct heterojunction photocatalysts (such as, TiO_2, ZnO, $BiPO_4$, ZnS and $SrTiO_3$) is a kind of effective method to obtain the enhanced visible light photocatalytic activity [46–51]. The heterostructure between g-C_3N_4 and semiconductor can efficiently separate photogenerated electron and hole to reduce the recombination of charge carries [52]. The band edge positions of the $KCa_2Nb_3O_{10}$ matches well with those of g-C_3N_4, which theoretically could promote the charge separation of the heterojunction photocatalyst and thus enhance the photocatalytic activity. To the best of our knowledge, the coupling of ultrathin $KCa_2Nb_3O_{10}$ nanosheets with g-C_3N_4 nanosheets to obtain high visible light photocatalytic activity has not been reported previously.

Based on the above considerations, in the present study, we designed and constructed a unique 2D-2D heterostructure by coupling the ultrathin $K^+Ca_2Nb_3O_{10}^-$ nanosheets with g-C_3N_4 nanosheets (donated as g-C_3N_4/$K^+Ca_2Nb_3O_{10}^-$). Such 2D-2D heterostructure provides a large contact area for fast interfacial charge separation as well as a broadening optical window for effective light harvesting. The photocatalytic performance of this 2D-2D heterostructure was investigated by degradation of tetracycline hydrochloride (a refractory antibiotic) under visible light irradiation. The results suggested that g-C_3N_4/$K^+Ca_2Nb_3O_{10}^-$ nanosheet heterojunctions displayed much higher photocatalytic activity under visible light irradiation than bare $K^+Ca_2Nb_3O_{10}^-$ and g-C_3N_4 nanosheets. The possible photocatalytic mechanism for the degradation of tetracycline hydrochloride over the heterojunction catalysts was also investigated. The construction of 2D-2D heterostructures with intimate contact opens up an effective strategy for the development of highly active visible light photocatalysts for environmental applications.

2. Experimental section

2.1. Materials

Calcium carbonate ($CaCO_3$), niobium(IV) oxide (Nb_2O_5), anhydrous potassium carbonate (K_2CO_3), potassium chloride (KCl), nitric acid (HNO_3), tetrabutylammonium hydroxide solution 10% (TBAOH 10 wt%), absolute ethanol and urea were purchased from Sinopharm Chemical Reagent Co., Ltd., China and were used as received without any further purification. Deionized water was used throughout the experiments.

2.2. Catalyst preparation

2.2.1. Synthesis of ultrathin $K^+Ca_2Nb_3O_{10}^-$ nanosheets

$KCa_2Nb_3O_{10}$ (KCNO) was synthesized according to previous reports [17,53]. The raw materials K_2CO_3, $CaCO_3$, and Nb_2O_5 (K/Ca/Nb = 1.1:2:3) were put in an agate mortar and mixed using a pestle. The mixed powder was calcined at 1473 K for 12 h to get layered KCNO. The obtained powder KCNO was treated with 200 mL of HNO_3 aqueous solution to replace K^+ in the interlayer space with H^+. After 3 days, the acidic solution was replaced by a fresh one via decantation and refilling. After treatment for another 3 days, the resulting powder were collected by filtration and washed with a copious quantity of pure water, and then air-dried to get $HCa_2Nb_3O_{10}$ (HCNO) powder.

Exfoliation of the proton-exchanged material was performed using an aqueous solution of TBAOH at room temperature. The HCNO powder was shaken vigorously in 100 mL of TBAOH aqueous solution for 7 days. The molar ratio of TBAOH to exchangeable cations in the layered solids was 1.0. Additionally, the exfoliation process was under the assistance of sonication every day. The resulting colloidal suspension was added dropwise into 2 M KCl aqueous solution, immediately producing white precipitate. The precipitate (ultrathin $K^+Ca_2Nb_3O_{10}^-$ nanosheets) was thoroughly washed with water several times and dried in air at room temperature and the obtained sample was denoted as K^+CNO^- hereafter. The exfoliation process is shown in Scheme 1.
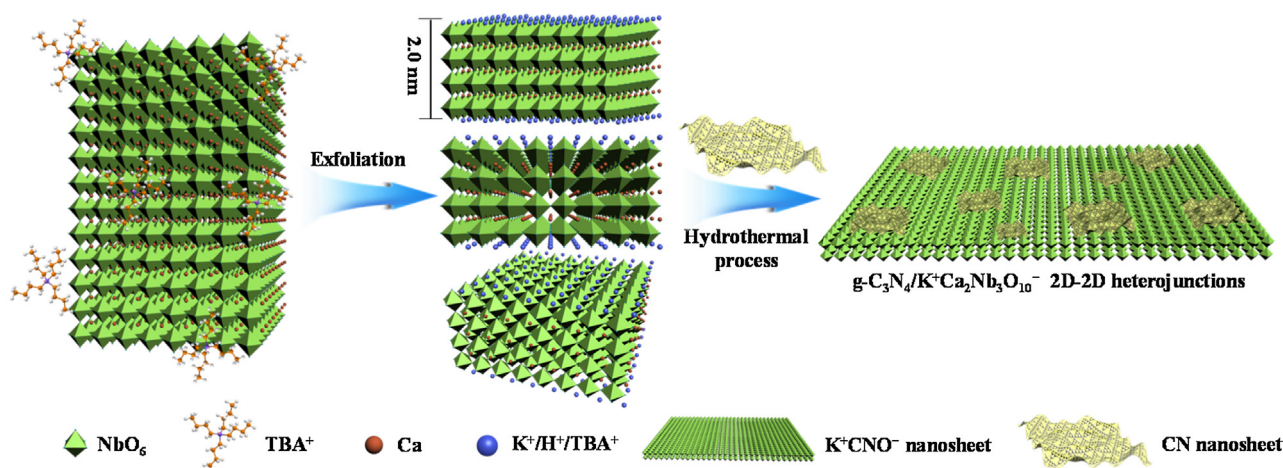
2.2.2. Preparation of g-C_3N_4 nanosheets

The g-C_3N_4 (abbreviated as CN) nanosheets were prepared by a thermal polymerization strategy [54]. In a typical synthesis, 12 g of urea was put into an alumina crucible with a cover, and then heated at 823 K for 4 h at the rate of 2.3 K min^{-1} in a tube furnace for 4 h in air. The resultant yellow powder was used in the subsequent studies.

2.2.3. Fabrication of the CN/K^+CNO^- nanosheet heterojunctions

The CN/K^+CNO^- nanosheet heterojunctions were fabricated by a facile one-step hydrothermal approach (as shown in Scheme 1). Briefly, 50 mg of K^+CNO^- nanosheets and a certain amount of the as-prepared CN were added in 65 mL deionized water kept stirring for 30 min. Then the mixture was well dispersed by sonication for 30 min and then the result homogeneous suspension was transferred into an autoclave, followed by hydrothermal treatment at 140 °C for 12 h. The resulting products were collected by centrifugation and subsequently washed with deionized water and anhydrous ethanol several times. The final products were obtained after drying at 60 °C for 24 h. To investigate the role of the nanosheet heterojunctions in the photocatalytic performances, the amount of CN and K^+CNO^- were varied to obtain CN/K^+CNO^- nanosheet heterojunctions with mass ratios of 10%, 20%, 30% and 40%, which were denoted as 10-CN/K^+CNO^-, 20-CN/K^+CNO^-, 30-CN/K^+CNO^- and 40-CN/K^+CNO^-, respectively.

2.3. Catalysts characterization

The prepared samples were characterized by X-ray diffraction pattern (XRD, XRD-6100, Shimadzu) with Cu-Kα radiation (λ = 1.54 Å), transmission electron microscopy (TEM, FEI JEM-2100, JEOL), Fourier transform infrared spectra (FT-IR, Nicolet Model Nexus 470), Atomic force microscopy (AFM, MFP-30, Asylum Research), X-ray photoelectron spectroscopy analysis (XPS, ESCA PHI500), UV–vis diffuse reflectance spectra (DRS, UV-3600Plus, Shimadzu), photoluminescence spectra (PL, Cary Eclipse, Varian). The nitrogen adsorption-desorption isotherms at 77 K were researched using a TriStar II 3020 surface area and porosity analyzer (Micromeritics Instrument Corporarion, USA). The electron

Scheme 1. Fabrication process of the CN/K⁺CNO⁻ nanosheet heterojunctions.

spin resonance (ESR) signals of radicals spin-trapped by spin-trap reagent DMPO (Sigma Chemical Co.) in water or methanol were examined on a Bruker model ESR JES-FA200 spectrometer. The intermediates analysis was performed by a high performance liquid chromatography-mass spectrometry (HPLC–MS) system (Agilent 1290/6460, Triple Quad MS) equipped with a Zorbax XDB-C18 column (150×2.1 mm, 3.5μm). The mobile phase was a methanol aqueous solution (40:60, V/V) with a flow rate of 1.0 mL min^{-1} and the column temperature was $30\,^{\circ}$C.

2.4. Photocatalytic performance

The photocatalytic activities of the samples were first evaluated by degradation of tetracycline hydrochloride (TC) in an aqueous solution (35 mg/L) under irradiation of a 500 W tungsten lamp. 40 mg of the photocatalysts was added into the 40 mL TC aqueous solution in a Pyrex reactor at room temperature under air. The dispersion was stirred in the dark for 90 min to reach the adsorption equilibrium. Then the visible light was turn on for the photodegradation tests. 4 mL of the sample solution were taken at given time intervals and separated by centrifugation. The concentration of TC during the degradation was monitored by a UV–vis spectrophotometer (Cary 8454, Agilent).

2.5. Photoelectrochemical measurement

All of the electrochemical measurements were performed in a three-electrode system on an electrochemical workstation (CHI660B). Typically, 4 mg of catalyst and 20 μL Nafion solution (5 wt%) were dispersed in 1 mL ethanol by sonicating for 1 h to form a homogeneous ink. Then, 30 μL of the resulting colloidal dispersion was dropped onto a piece of FTO glass (1×1 cm^2). The prepared sample was used as the working electrode, a Pt wire as the counter electrode, and Ag/AgCl as a reference electrode. A 500 W Xe arc lamp served as a light source. The photocurrent and electrochemical impedance spectroscopy (EIS) was performed in 0.2 M Na$_2$SO$_4$ aqueous solution and 0.1 M KCl solution containing 5 mM [Fe(CN)$_6$$^{3-}$/Fe(CN)$_6$$^{4-}$], respectively.

3. Results and discussion

3.1. Structures and morphologies of as-prepared samples

The XRD patterns of the as-prepared KCNO, HCNO and ultrathin K⁺CNO⁻ nanosheets are firstly shown in Fig. 1. The original KCNO (Fig. 1a) exhibits strong and sharp diffraction peaks, corre-
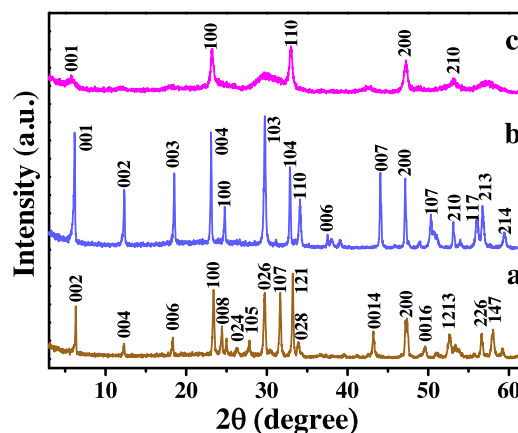

Fig. 1. XRD patterns of (a) KCNO, (b) HCNO, (c) K⁺CNO⁻.

sponding well to (00n) facets as previously reported [14,18]. No impurities were detected in the sample. In Fig. 1b, the (00n) diffraction peaks of HCNO (JCPDS card No. 40-0884) shifted to lower angles after the proton exchange and agreed well with the previously reported data [25]. Fig. 1c shows the XRD pattern of ultrathin K⁺CNO⁻ nanosheets and all general lines (*hkl*) are absent, indicating the loss of three-dimensional order. In addition, the intensities of peaks corresponding to (001), (002), (003) significantly decreased and the peak width of (100), (103), (110), (200) peaks broadened obviously after the exfoliation process [55]. The XRD profile of the ultrathin K⁺CNO⁻ nanosheets agrees well with the previously reported results [56,57].

In order to further investigate the phase structure of the ultrathin K⁺CNO⁻ nanosheets in the heterojunction systems, the as-prepared CN/K⁺CNO⁻ nanosheet heterojunctions as well as CN nanosheets were analyzed by XRD (Fig. 2). For comparison purpose, the XRD pattern of the pure K⁺CNO⁻ nanosheets is shown in Fig. 2a. In the case of pure CN (Fig. 2f), two characteristic peaks at 13.04° and 27.2° correspond to the (100) and (002) planes of the graphite-like carbon nitride arising from the interlayer structural packing and the characteristic interplanar staking peaks of aromatic systems, respectively [57]. By comparing the curves of CN/K⁺CNO⁻ nanosheet heterojunctions (Fig. 2b–e), it can be found that the diffraction peaks intensity of CN show a relatively decrease in the heterojunction systems. The main reason could be ascribed to the overlap of the primary peak of CN (27.2°) with the board diffraction peak of K⁺CNO⁻ (29.64°). No other impurity peaks were
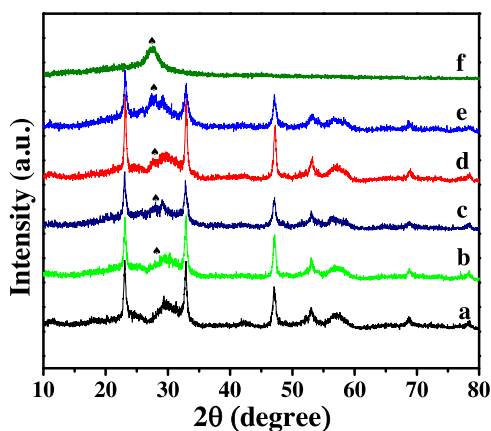
Fig. 2. XRD patterns of (a) K^+CNO^-, (b) 10-CN/K^+CNO^-, (c) 20-CN/K^+CNO^-, (d) 30-CN/K^+CNO^-, (e) 40-CN/K^+CNO^-, and (f) CN.
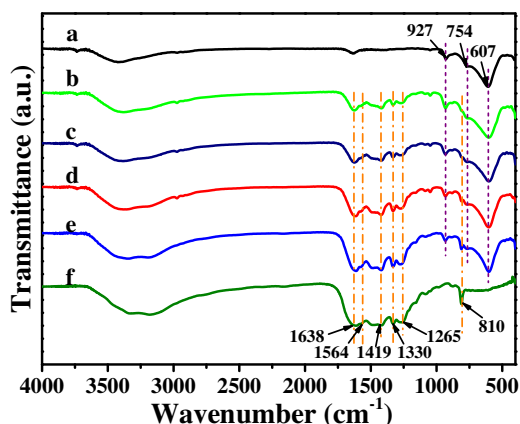

Fig. 3. FT-IR spectra of (a) K^+CNO^-, (b) 10-CN/K^+CNO^-, (c) 20-CN/K^+CNO^-, (d) 30-CN/K^+CNO^-, (e) 40-CN/K^+CNO^-, and (f) CN.

detected in the XRD pattern, which confirmed the high purity of the CN/K^+CNO^- nanosheet heterojunctions.

FT-IR spectra are carried out to further determine the presence of CN nanosheets in the CN/K^+CNO^- nanosheet heterojunctions. As shown in Fig. 3a, absorption peaks appearing at 607, 754 and 929 cm^{-1} are assigned to the characteristic internal Nb—O stretching vibration in the NbO_6 octahedron [25,58]. In the case of pure CN (Fig. 3f), the sharp band at 810 cm^{-1} is originated from the breathing of the tri-s-triazine units [59]. A series of peaks found in the range of 1700–1000 cm^{-1} is attributed to the stretching modes of CN heterocycles [60]. In addition, the broad bands between 3000 and 3300 cm^{-1} originate from the secondary and primary amines [60–62]. In the case of CN/K^+CNO^- nanosheet heterojunctions, the main characteristic peaks of K^+CNO^- and CN could be clearly observed in the FT-IR spectra (Fig. 3b–e), implying that no structural changes of K^+CNO^- occurred during the hybridization process.

XPS analysis was performed to further determine the elemental compositions and chemical status of the as-prepared catalysts. The full scan survey XPS spectrum of the 20-CN/K^+CNO^- nanosheet heterojunction clearly confirms the presence of K, Nb, Ca O, C and N elements (Fig. 4a). As can be seen from Fig. 4b, the characteristic peaks of Ca^{2+}, located at about 346.4 and 350.0 eV, are assigned to the Ca $2p_{3/2}$ and Ca $2p_{1/2}$ binding energies, respectively [63]. In Fig. 4c, two peaks at 206.6 and 209.3 eV could be separately attributed to Nb $3d_{5/2}$ and Nb $3d_{3/2}$, respectively. Meanwhile, the main peak located at 529.5 eV is ascribed to the O 1s binding energy (Fig. 4d). Notably, when CN was combined with the ultrathin K^+CNO^- nanosheets, the Ca 2p, Nb 3d and O 1s peaks for

20-CN/K^+CNO^- display a slight shift towards higher binding energy compared to pure K^+CNO^-. The shifts could be due to the presence of strong interfacial interaction at the interfaces between the ultrathin K^+CNO^- nanosheets and CN nanosheets [64].

The formation of the nanosheet heterojunction was further confirmed by analysis of the high-resolution C 1s and N 1s spectra in Fig. 4e and f. The C 1s spectrum of CN can be divided into two peaks centered at 284.7 and 288.3 eV (Fig. 4e). The former peak is assigned to standard reference carbon, while the latter peak is identified as the sp^2-bonded carbon in CN network [59]. In Fig. 4f, the dominant peak of N 1s spectrum located at 397.8 eV is ascribed to the sp^2-bonded nitrogen in triazine rings (C—N=C) [65]. It is worth noting that both the peaks of C 1s and N 1s for the 20-CN/K^+CNO^- shift toward the higher binding energies, which was driven from the probable electron transfer and delocalization of firmly contacted CN and the ultrathin K^+CNO^- nanosheets [66]. These shifts in the binding energies of the 20-CN/K^+CNO^- clearly indicating that there is strong interfacial interaction between K^+CNO^- and CN in the heterojunction.

The thickness of the ultrathin K^+CNO^- nanosheets was measured by AFM analysis, as exemplified by a typical image of nanosheets deposited on a mica wafer substrate (Fig. 5a and b). The majority of the nanosheets observed have lateral sizes of about a few hundreds of nanometers and the average thickness of the middle part of K^+CNO^- nanosheets is in the range of 2.0–2.1 nm. The thickness of the edge part shows slightly higher, originating from water molecules selectively gathered at the edge part [67]. This result is similar with other perovskite-type nanosheets reported previously [10,14]. The ultrathin K^+CNO^- nanosheets prepared in this work provided an excellent platform to construct the CN/K^+CNO^- nanosheet heterojunctions.

Further information about the microstructure and morphologies of the CN/K^+CNO^- nanosheet heterojunctions along with bare K^+CNO^- and CN nanosheets were obtained from TEM and high-resolution TEM (HRTEM) image analysis (Fig. 6). As shown in Fig. 6a, the TEM image for the bare K^+CNO^- sample shows the ultra-thin lamellar nanosheet morphology. The lateral dimensions of the nanosheets are approximately a few hundreds of nanometers, which is in agreement with the AFM measurements. As shown in Fig. 6b, the CN nanosheets exhibit wrinkled lamellar morphology with obvious pores and wrinkles structure, which are created by the thermal polymerization of urea. Fig. 6b–f showed the TEM images CN/K^+CNO^- nanosheet heterojunctions with different content of CN nanosheets. In comparison with the bare K^+CNO^-, when CN was combined with the ultrathin K^+CNO^- nanosheets, the nearly transparent nanosheets become blur, indicating that the CN nanosheets integrate compactly on the surface of ultrathin K^+CNO^- nanosheets to construct a well-defined sheet-on-sheet structure. The HRTEM image of the 20-CN/K^+CNO^- nanosheet heterojunction exhibits the distinct lattice fringes of 0.279 nm, corresponding to the (110) plane of K^+CNO^- nanosheets (Fig. 6g).

The composition and microstructure of 20-CN/K^+CNO^- samples were further investigated by high-angle annular dark-field scanning transmission electron microscopy (HAADF-STEM) and energy dispersive X-ray spectroscopy (EDS) elemental scanning (Fig. 6h). The STEM image and the EDS elemental mapping from this area displayed a homogeneous distribution of K, Ca, Nb, O, C and N elements in the 20-CN/K^+CNO^- nanosheet heterojunction. Noticeably, the mapping image of K, Ca, Nb and O shows the same shape. Meanwhile, it can be clearly seen that C and N elements originated from CN nanosheets distributed evenly on the surface of K^+CNO^- nanosheets. These results give strong evidence that the 20-CN/K^+CNO^- nanosheet heterojunction was successful constructed.

The porosity and surface area of K^+CNO^-, CN and the 20-CN/K^+CNO^- nanosheet heterojunction were investigated through the N$_2$ adsorption-desorption isotherms method. As displayed In
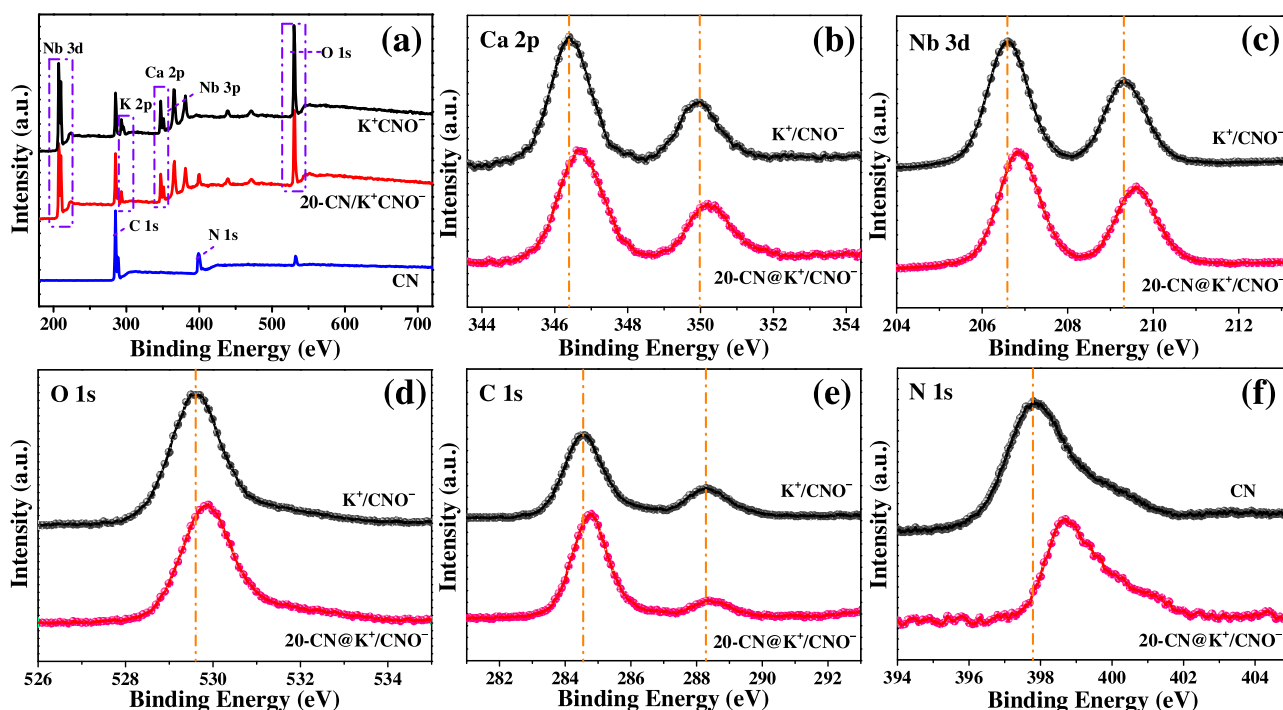
Fig. 4. XPS spectra of the pure K⁺CNO⁻, CN and 20-CN/K⁺CNO⁻ nanosheet heterojunction: (a) survey spectrum, (b) Ca 2p, (c) Nb 3d, (d) O 1s, (e) C 1s, and (f) N 1s.
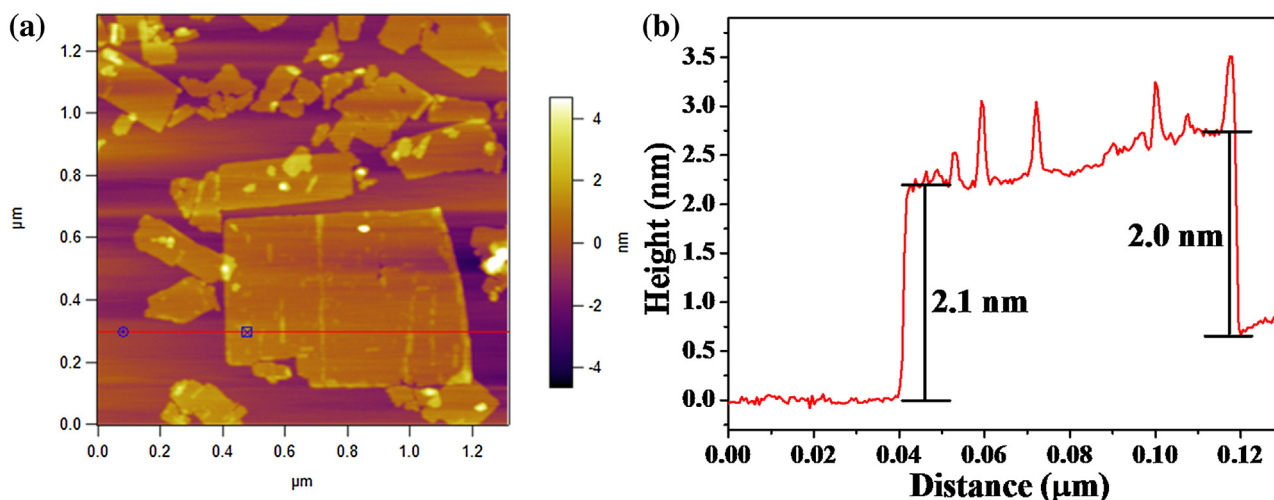

Fig. 5. (a) AFM image and (b) cross-section profile of ultrathin K⁺CNO⁻ nanosheets.

Fig. 7, a typical type IV isotherm featuring a pronounced H3-type hysteresis loop according to the IUPAC classification indicated the presence of micropores and mesopores within the composites [68]. The Brunauer-Emmett-Teller (BET) specific surface area was calculated to be 77.68 m² g⁻¹ for the 20-CN/K⁺CNO⁻ nanosheet heterojunction, which is much larger than that of pure K⁺CNO⁻ (50.89 m² g⁻¹) and CN (33.75 m² g⁻¹). Accordingly, it can be found that when CN nanosheets was introduced on the surface of K⁺CNO⁻ nanosheet, the surface area of the formed nanocomposites show an obviously improvement compared with the bare K⁺CNO⁻ nanosheet. The improved specific surface area is beneficial for absorbing more active species and reactants on the surface, which could be advantageous to the improvement of the photocatalytic activity [69].

3.2. Photocatalytic activity

The photocatalytic performances of K⁺CNO⁻, CN and the heterojunction samples for degradation of TC (35 mg/L) were evaluated under visible light irradiation. Before the photocatalytic performance test, the CN were treated by hydrothermal treatment at 140 °C for 12 h. As shown in Fig. 8a, it is notable that the absorption-desorption balance has been achieved between the catalyst and TC solution within 90 min in the dark. In the control experiment, the TC concentration remained unchanged over time in the absence of catalysts, demonstrating that TC is quite stable and excluding the possibility of the self-photolysis process of TC. It can be found that only 12.2% and 45.9% of TC were degraded using the K⁺CNO⁻ and CN nanosheets within 90 min, respectively. Surprisingly, com-
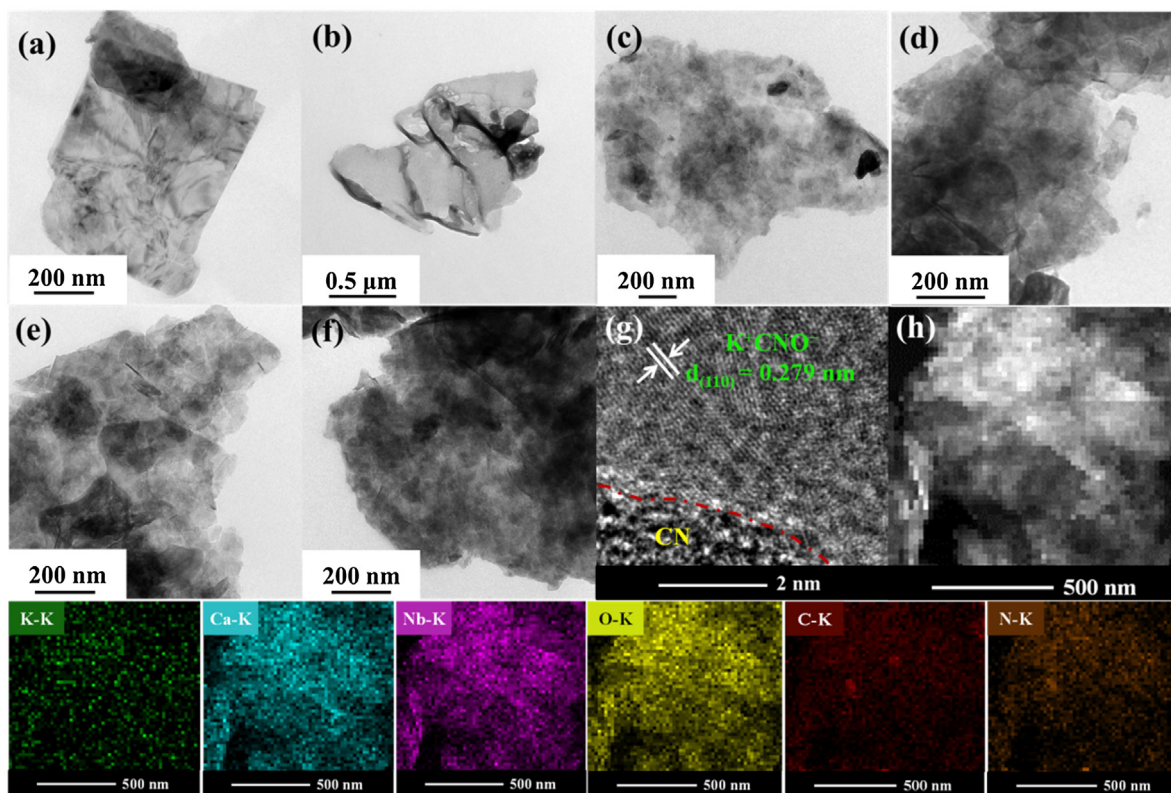
Fig. 6. TEM images of (a) K^+CNO^-, (b) CN, (c) 10-CN/K^+CNO^- (d) 20-CN/K^+CNO^-, (e) 30-CN/K^+CNO^-, (f) 40-CN/K^+CNO^-, (g) HRTEM image of 20-CN/K^+CNO^-, (h) HAADF-STEM image and the corresponding EDS elemental mapping images of the 20-CN/K^+CNO^- nanosheet heterojunction.
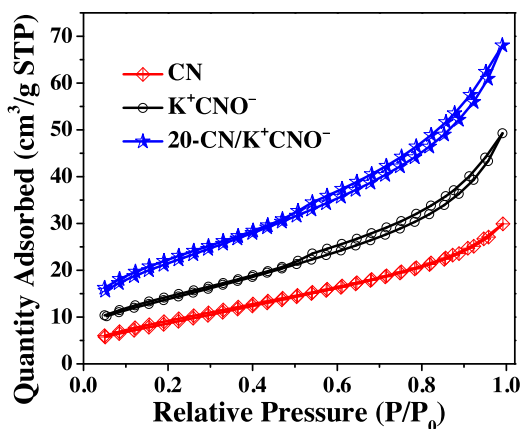

Fig. 7. Nitrogen absorption-desorption isotherms of K^+CNO^-, CN and 20-CN/K^+CNO^- samples.

bining the K^+CNO^- and CN nanosheets resulted in a significantly enhanced efficiency for the degradation of TC. The as-prepared 20-CN/K^+CNO^- nanosheet heterojunction showed the optimal activity and no enhancement was observed with further increasing the content of CN of up to 40%. The 20-CN/K^+CNO^- sample could degrade 81% of TC in 90 min. Meanwhile, the corresponding TC degradation kinetic curves over the as-prepared catalysts were shown in Fig. 8b and c. It can be found that the reaction rate constant values of pure K^+CNO^- ($0.00208 \, min^{-1}$) and CN ($0.00759 \, min^{-1}$) are much lower than that of the 20-CN/K^+CNO^- sample ($0.0137 \, min^{-1}$).

The stability of the 20-CN/K^+CNO^- nanosheet heterojunction was also investigated by recycling the photocatalyst for the degradation of TC under visible light irradiation. It is clearly shown in Fig. 8d that there is no apparent deactivation on the photocat-

alytic performance after four consecutive runs, indicating that the as-prepared 20-CN/K^+CNO^- nanosheet heterojunction exhibits an excellent catalytic stability and high performance for the treatment of TC.

Direct detection of reactive intermediates could give important information for the investigation of the photocatalytic degradation mechanism of TC. HPLC–MS was employed precisely to identify the intermediates. As shown in Fig. 9, it demonstrated that the intensity of the TC peak decreased with the process of the reaction. It can be observed directly that TC at m/z 445.5 eluted at a retention time of 7.31 min (Fig. 10a). And the main intermediates were observed in Fig. 10b–d. The intensity of TC peak decreased during the reaction process, whereas the intensity of intermediates peaks increased after 30 min irradiation (Fig. 10b). Some main intermediates with m/z of 416, 402, 398 and 350 were generated. The intermediate was produced by losing the *N*-methyl group or hydroxyl group of TC molecule [70,71]. After reaction for 60 min, more such groups detached from TC molecules and lots of intermediates chromatograms were generated in Fig. 10c ($m/z = 333$, 279, 234, 209, 149). As the reaction continued, the deprotonated TC molecular ion with $m/z = 445$ completely disappeared and the intensities of the generated intermediates decreased evidently after 90 min (Fig. 10d). These results demonstrated that the intermediates engendered in the photocatalytic degradation were degraded in succession after a period of photodegradation time [72,73]. The proposed photocatalytic degradation pathway of TC over 20-CN/K^+CNO^- heterojunction is shown in Fig. 11.

3.3. Optical and electronic properties

The optical properties of the as-prepared catalysts were probed by UV–vis DRS. The absorption spectra are shown in Fig. 12a, the ultrathin K^+CNO^- nanosheets exhibited intense optical absorption
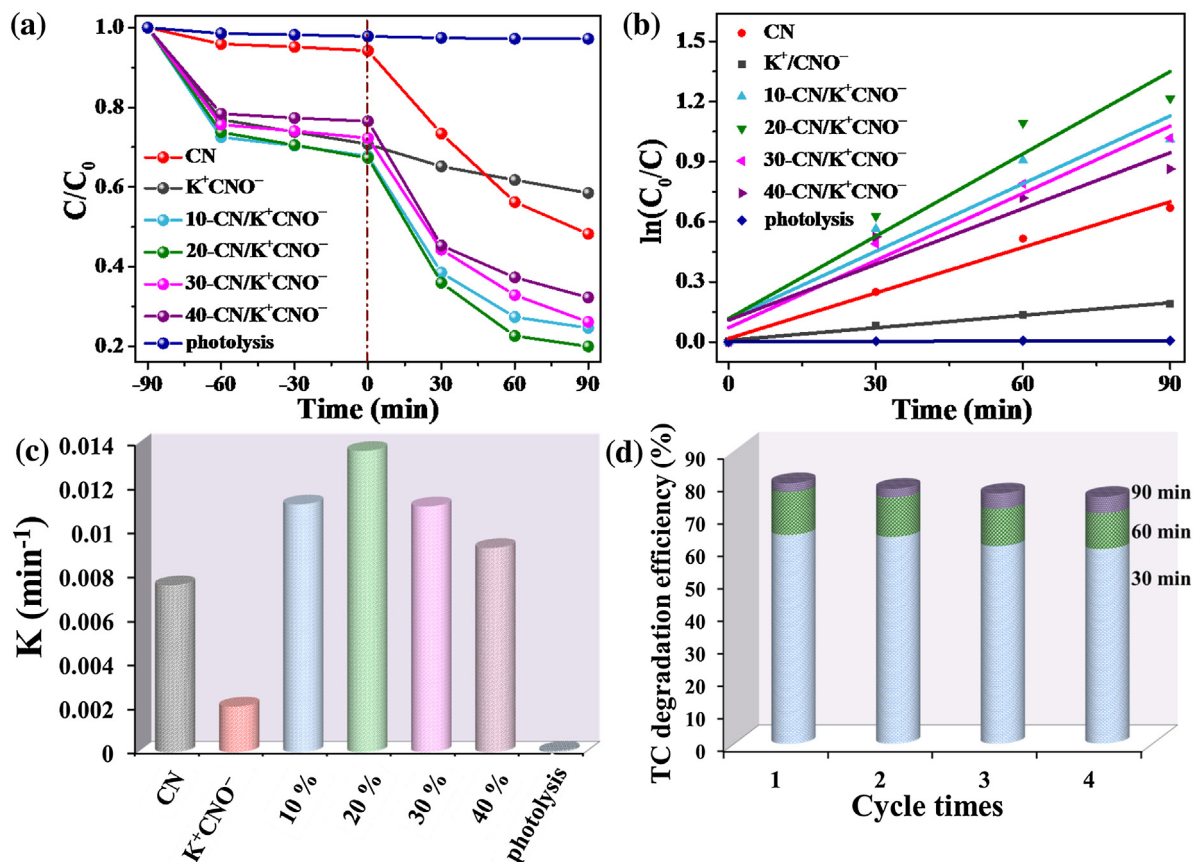
Fig. 8. (a) Photocatalytic degradation efficiency of TC (35 mg/L) under visible light irradiation over K⁺CNO⁻, CN and the nanosheet heterojunctions, (b and c) kinetic curves and reaction rate constant for TC degradation over the as-prepared photocatalysts, (d) Cycling runs for degradation efficiency of the TC over the 20-CN/K⁺CNO⁻ nanosheet heterojunction under visible light irradiation.
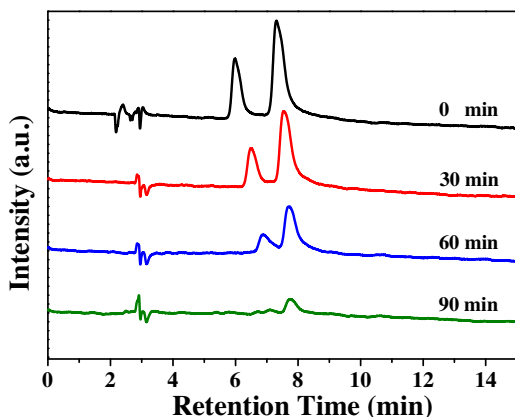

Fig. 9. HPLC–MS chromatograms of TC degradation over 20-CN/K⁺CNO⁻ sample under visible-light irradiation.

onset which is located at around 360 nm. While the absorption edge of CN nanosheets is located at about 450 nm. In comparison with bare K⁺CNO⁻, when CN content in the CN/K⁺CNO⁻ nanosheet heterojunctions increased, all heterojunction samples show enhanced absorption in the visible light range accompanying a red shift in the absorption edge. This situation could be attributed to the synergistic effect between K⁺CNO⁻ and CN nanosheets. These optical results demonstrated that the as-prepared CN/K⁺CNO⁻ heterojunction could be excited by visible light, leading to generate more electron-hole pairs and exhibit the favorably enhanced visible-light photocatalytic performance.

Typically, the band gap energies of K⁺CNO⁻ and CN nanosheets could be estimated by the following equation [74]:

$$\alpha h\nu = A \cdot (h\nu - E_g)^{n/2} \tag{1}$$

where a, hν, E$_g$, A, and n are the absorption coefficient, incident light frequency, band gap, constant, and an constant, respectively. In the equation, n represents the optical-transition type of semiconductors (n is 1 for direct transitions and 4 for indirect transitions). The integer n is 4 for both K⁺CNO⁻ and CN nanosheets [10,58]. As shown in Fig. 12b, the band gap energies of the K⁺CNO⁻ and CN nanosheets were estimated from the plots of ($\alpha h\nu$)$^{1/2}$ versus hν. Accordingly, the E$_g$ of the K⁺CNO⁻ and CN nanosheets are calculated to be 3.38 and 2.71 eV, respectively. These results are in good agreement with the reported data [25,75].

It is well acknowledged that the photoluminescence emission mainly results from the recombination of photoexcited electron-hole pairs. A higher PL intensity indicates a higher recombination rate of photoexcited electron-hole pairs [76]. Fig. 13a exhibits the PL emission spectra of pure K⁺CNO⁻ and the CN/K⁺CNO⁻, in which all the samples show a strong emission peak centered at around 430 nm with an excitation wavelength of 320 nm. The inset shows the bare CN and 20-CN/K⁺CNO⁻ exhibit strong photoluminescence at room temperature centered at 445 nm with an excitation wavelength of 380 nm. Remarkably, the PL intensities of CN/K⁺CNO⁻ samples decrease obviously when CN was introduced into this system, indicating that the recombination of free charge carriers is prevented effectively in the nanosheet heterojunctions. The 20-CN/K⁺CNO⁻ sample shows the lowest PL intensity compared with
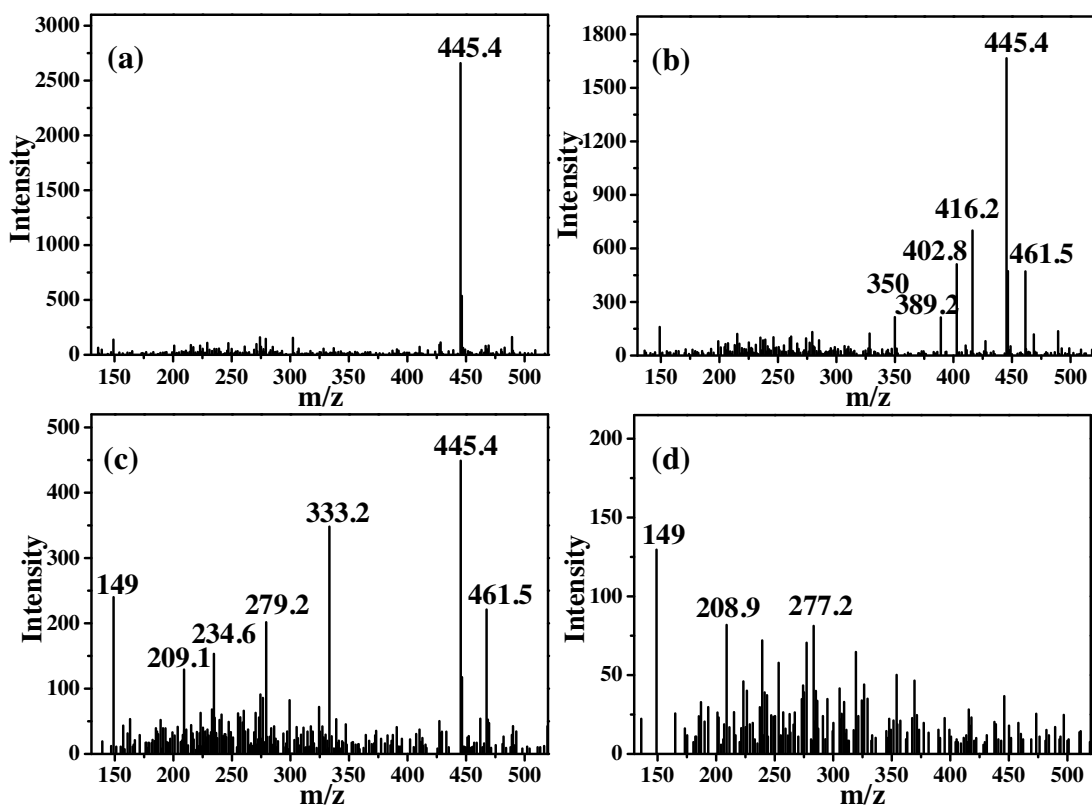
Fig. 10. HPLC–MS spectra of the TC intermediates eluted at different reaction time of (a) 0 min, (b) 30 min, (c) 60 min and (d) 90 min.
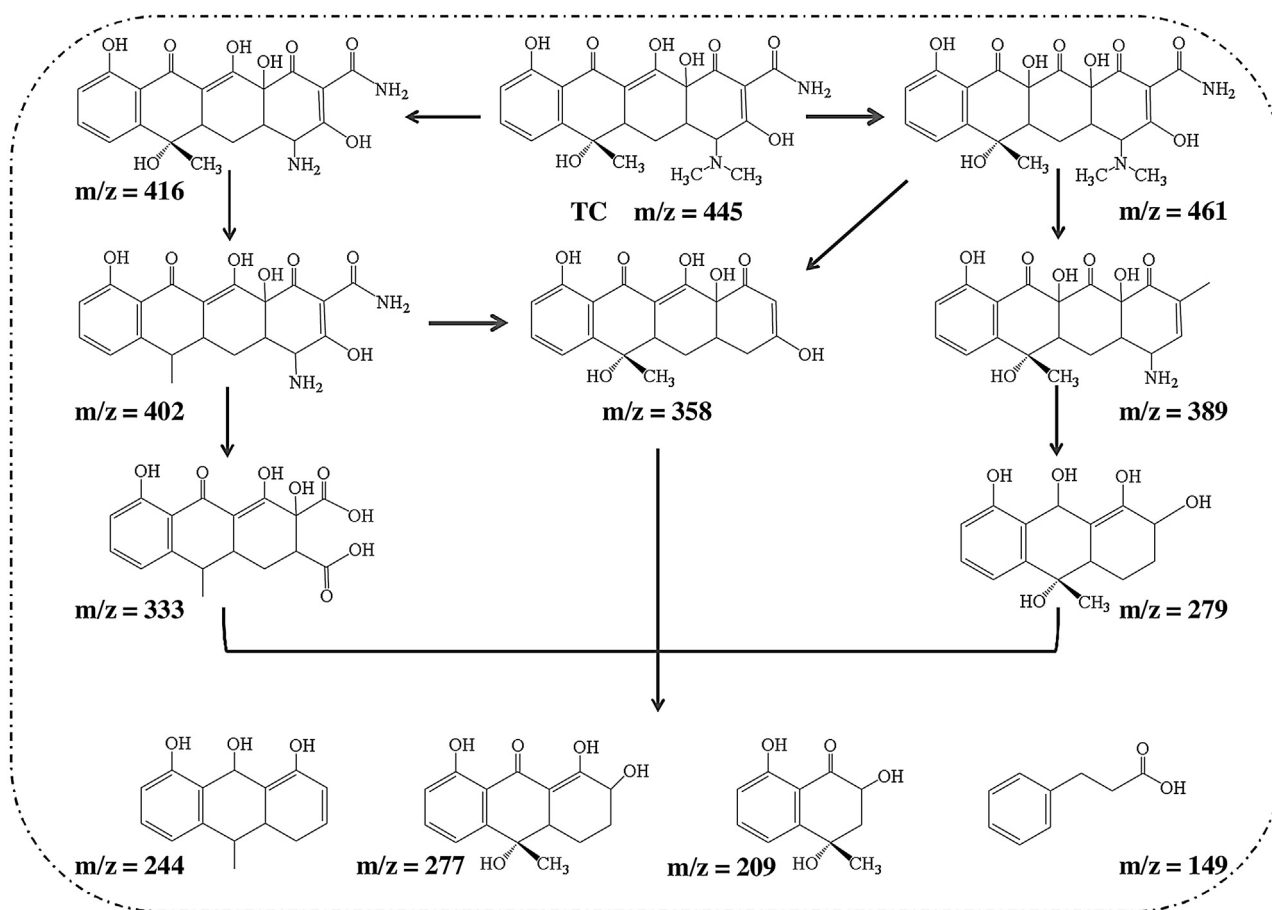

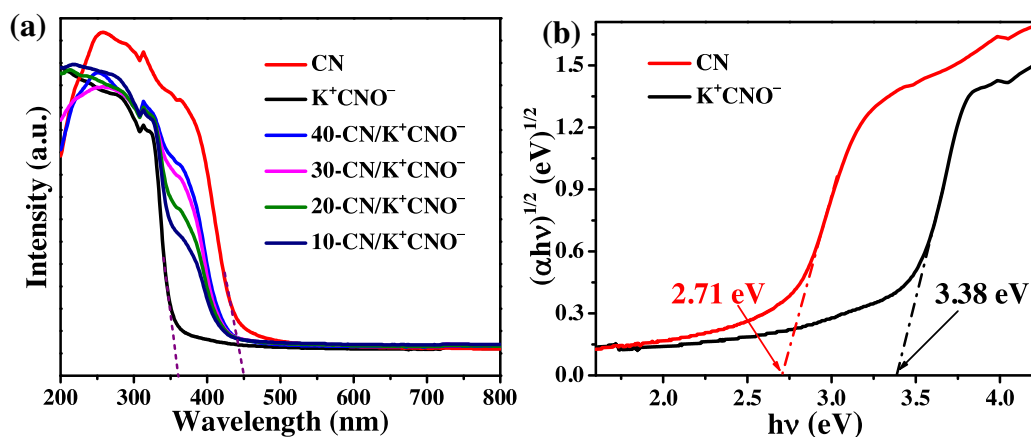**Fig. 11.** The proposed photocatalytic degradation pathway of TC.

Fig. 12. (a) UV–vis diffuse reflectance spectra of different samples, (b) Plot of $(\alpha h\nu)^{1/2}$ versus $h\nu$ for the band gap energy of K^+CNO^- and CN nanosheets.
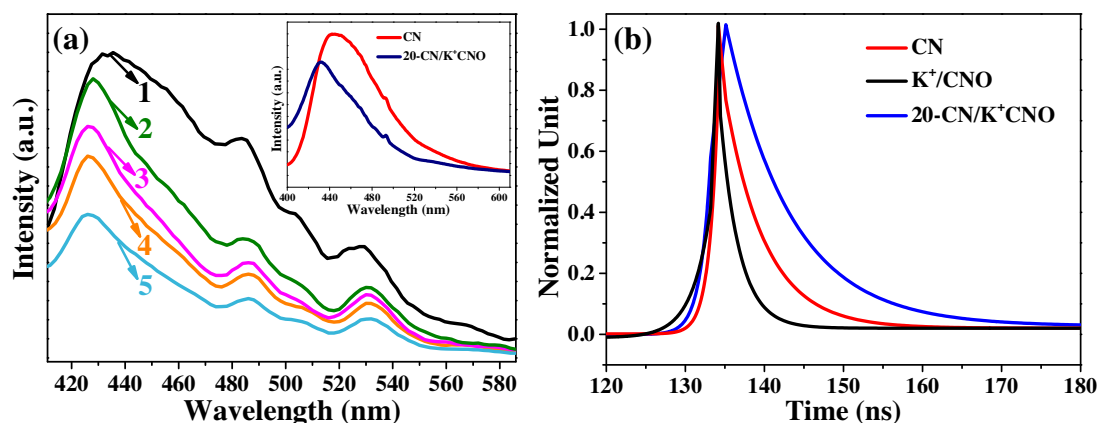

Fig. 13. (a) PL spectra of as-prepared catalysts: (1) K^+CNO^-, (2) $40\text{-}CN/K^+CNO^-$, (3) $10\text{-}CN/K^+CNO^-$, (4) $30\text{-}CN/K^+CNO^-$, (5) $20\text{-}CN/K^+CNO^-$; (b) time-resolved fluorescence decay spectra of as-prepared catalysts.

all the other samples, which is consistent with the highest photocatalytic performance among all the samples.

To better understand the recombination process in CN/K^+CNO^- heterojunction, we performed time-resolved photoluminescence experiments, and the normalized decay profiles are shown in Fig. 13b. The fluorescence lifetime of bare CN, K^+CNO^- and $20\text{-}CN/K^+CNO^-$ are 2.398, 5.067 and 8.181 ns, respectively. Consequently, the $20\text{-}CN/K^+CNO^-$ nanosheet heterojunction showed a longer lifetime compared with the bare CN and K^+CNO^-. The prolonged lifetime may originate from the formation of CN/K^+CNO^- nanosheet heterojunction, which efficiently reduced the recombination of photogenerated electrons and holes [77].

Electrochemistry analysis was further applied to explore the separation, migration, and trapping of photogenerated charge carriers [7]. The photocurrent responses were used to investigate the efficiency of charge carrier transfer and separation as the photocurrent response results from the segregation of free charge carriers [78]. As shown in Fig. 14a, the transient photocurrent responses of as-prepared catalysts electrodes with light-on and light-off were carried out using a typical three-electrode system in a 0.2 M Na_2SO_4 aqueous solution. The outstanding photocurrent density implies that the construction of the $20\text{-}CN/K^+CNO^-$ nanosheet heterojunction facilitates considerable excitation of the carriers. The displayed photocurrent density of the $20\text{-}CN/K^+CNO^-$ sample is almost 1.5-fold as high as that of pure K^+CNO^-. In the case of pure CN, its photocurrent density is less than half of $20\text{-}CN/K^+CNO^-$. These results demonstrate that the ultrathin K^+CNO^- nanosheets with intimate contact of CN nanosheets can facilitate

an effective separation of photogenerated electron-hole pairs and accelerate interfacial charge transfer [79].

To gain deeper insight into the electron transfer mechanism in the heterojunction system, the electron transport and recombination properties of the pure K^+CNO^-, CN and $20\text{-}CN/K^+CNO^-$ nanosheet heterojunction were investigated by EIS analysis, and the results are shown in Fig. 14b. Generally, a smaller arc in an EIS Nyquist plot indicates a lower charge-transfer resistance on the electrode surface [80]. The $20\text{-}CN/K^+CNO^-$ nanosheet heterojunction exhibits lower charge transfer resistance than that of bare K^+CNO^- and CN nanosheets, suggesting that effective shuttling of charges between the electrode and the electrolyte, and faster interfacial charge transfer occurred on the interface of $20\text{-}CN/K^+CNO^-$ owing to the formation of the heterojunction.

3.4. Possible photocatalytic mechanism

To study the active species in the heterojunction system, the species trapping experiments were performed during the degradation of TC over $20\text{-}CN/K^+CNO^-$ nanosheet heterojunction. The results are shown in Fig. 15. When *tert*-butyl alcohol (*t*-BuOH, scavenger of hydroxyl radical •OH) [81] was added, the degradation of TC was hardly affected, indicating that the •OH was not the main active species. However, the decomposition rate decreased somewhat when the ammonium oxalate (AO) (quencher of h^+) was added into the reaction system [82], which indicated that h^+ plays an important role in the degradation process. Prominently, with the addition of *p*-benzoquinone (BQ, $O_2^{\bullet-}$ scavenger), the degra-
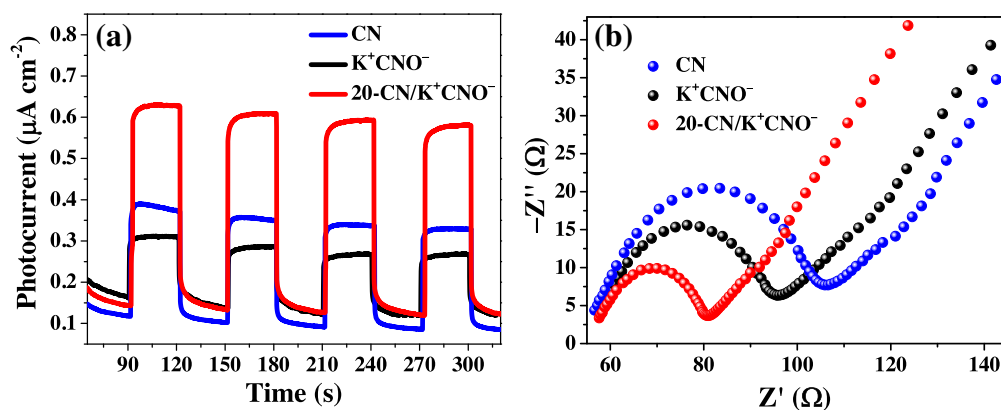
Fig. 14. (a) Transient photocurrent response and (b) Nyquist plots of EIS for K^+CNO^-, CN and $20-CN/K^+CNO^-$ nanosheet heterojunction.
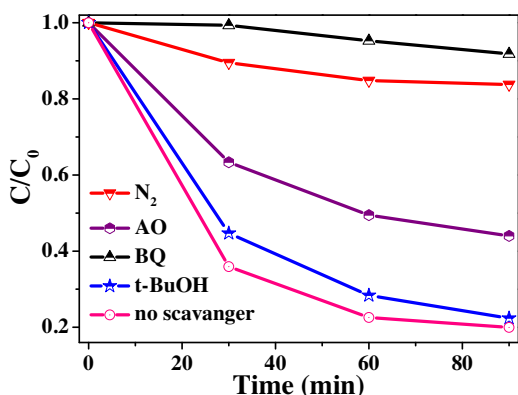

Fig. 15. Trapping experiment of the active species for the degradation of TC over the $20-CN/K^+CNO^-$ nanosheet heterojunction.

dation efficiency was inhibited drastically, revealing that $O_2^{\bullet-}$ are the dominant active species for the photocatalytic degradation of TC. Moreover, the controlled experiment in a N_2 atmosphere exhibited a remarkable decrease of the degradation efficiency. This result implies that O_2 could primarily act as efficient electron traps to generate $O_2^{\bullet-}$. Consequently, these above results reveal that h^+ and $O_2^{\bullet-}$ are the predominant active species in the TC degradation process over the $20-CN/K^+CNO^-$ nanosheet heterojunction.

In order to confirm the presented photocatalytic mechanism in depth, the main active species generated during the photocataly-

sis process was probed by spin-trapping ESR technique. As shown in Fig. 16a, the characteristic peaks of DMPO-$O_2^{\bullet-}$ were obviously observed in methanol dispersion of $20-CN/K^+CNO^-$ nanosheet heterojunction under visible light irradiation. And no such signals were detected in dark. However, in Fig. 16b, the characteristic peaks corresponding to the DMPO-$^{\bullet}OH$ adduct did not show up even under the visible light irradiation. The ESR results indicate that the $O_2^{\bullet-}$ radicals were produced during the photocatalytic reaction, while no $^{\bullet}OH$ radicals can be generated in this system, which are consistent with the above active species trapping experimental results.

3.5. Possible photocatalytic mechanism

On the basis of the results and discussion, the enhancement of the photocatalytic activity of CN/K^+CNO^- nanosheet heterojunctions may primarily originate from the synergistic effect of K^+CNO^- and CN nanosheets associated with the formation of heterojunctions on the contact interface. According to the DRS experimental results, the band positions of K^+CNO^- can be calculated by the following empirical equation [83]:

$$E_{CB} = \chi - 0.5Eg + E^e \tag{2}$$

$$\chi = (\chi_{(A)}{}^a \cdot \chi_{(B)}{}^b \cdot \chi_{(C)}{}^c)^{1/(a+b+c)} \tag{3}$$

where $\chi_{(A)}$, $\chi_{(B)}$ and $\chi_{(C)}$ are the absolute electronegativity of constituent atoms A, B, and C, respectively. And the χ values for K^+CNO^- is estimated to be 5.346 eV. E_{CB} and E_g are the conduction band (CB) edge potential and the band gap energy of the semiconductor, respectively. E^e is a scale factor relating the reference electrode
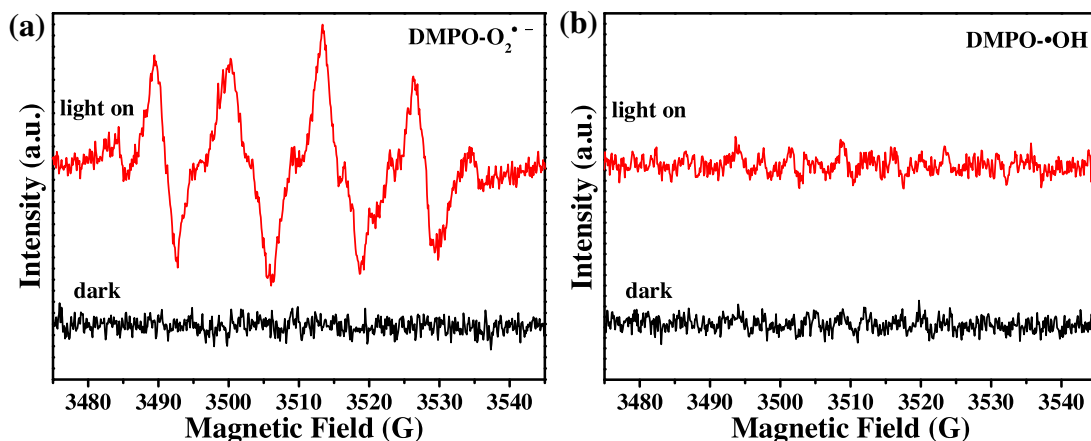

Fig. 16. DMPO spin-trapping ESR spectra recorded with $20-CN/K^+CNO^-$ (a) methanol dispersion (for DMPO-$O_2^{\bullet-}$) and (b) aqueous dispersion (for DMPO-$^{\bullet}OH$) under visible light irradiation.
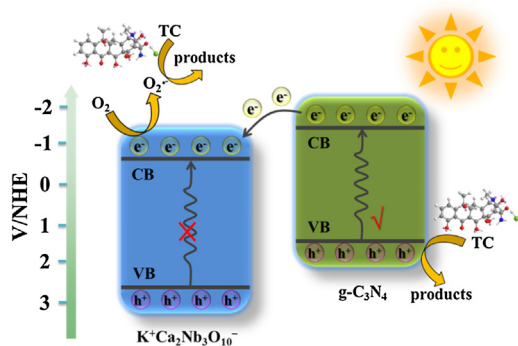
Fig. 17. Schematic illustrations of the possible separation and transfer of photogenerated electron-hole pairs in the CN/K$^+$CNO$^-$ nanosheet heterojunctions during TC degradation process under visible light irradiation.

redox level to the vacuum level (E^e = −4.44 eV for the normal hydrogen electrode). Meanwhile, the valence band (VB) edge potential (E_{VB}) can be calculated by the formula: $E_{CB} = E_{VB} - E_g$. Thus, the E_{CB} and E_{VB} of K$^+$CNO$^-$ are estimated to be −0.784 and 2.596 eV. In order to facilitate analyses, the schematic comparison regarding band edge positions of K$^+$CNO$^-$ and CN along with the standard potentials of relevant redox couples is shown in Fig. 17. When the CN/K$^+$CNO$^-$ nanosheet heterojunctions are irradiated with visible light, electrons are excited from the VB to the CB of CN nanosheets, leaving electropositive holes in the VB. The photogenerated electrons in the CN nanosheets tend to transfer to the ultrathin K$^+$CNO$^-$ nanosheets owing to that the CB edge potential of CN (−1.12 eV) is more negative than the CB edge potential of K$^+$CNO$^-$ (−0.784 eV) [36]. Simultaneously, the photogenerated holes of CN were left in the VB of CN due to the more positive VB edge (1.59 eV) of the CN [36]. Consequently, the CN/K$^+$CNO$^-$ nanosheet heterojunctions promoted the effective charge separation, resulting in enhanced photocatalytic activity eventually. Noticeably, it is in great agreement with the results of the PL, photocurrent, and EIS analysis. The photogenerated electrons accumulated in the CB of K$^+$CNO$^-$ mainly react with the adsorbed O$_2$ to generate O$_2$•$^-$ radicals due to the CB edge potential of K$^+$CNO$^-$ is more negative than the potential of O$_2$/O$_2$•$^-$ (−0.33 V vs. NHE) [61], which is responsible for the degradation and mineralization of organic pollutants in aqueous solution. Meanwhile, the corresponding photogenerated holes in the VB of CN can oxidize organic pollutants directly. Therefore, it can be concluded that the construction of CN/K$^+$CNO$^-$ heterojunction facilitates the efficient separation of photogenerated electron-hole pairs and thus accelerate the process of photocatalytic reaction.

4. Conclusion

In summary, we have successfully constructed a visible light active 2D-2D CN/K$^+$CNO$^-$ heterojunction that showed highly enhanced visible photocatalytic activity for TC degradation. The 20-CN/K$^+$CNO$^-$ shows the optimal efficiency of TC degradation (81%) and its degradation rate constant was about 6.6 and 1.8 times higher than that of bare K$^+$CNO$^-$ and CN, respectively. The formation of 2D-2D heterojunctions with effective charge transfer across substantial heterojunction interface was the main factor contributing to the enhancement of photocatalytic activity for CN/K$^+$CNO$^-$ nanosheet heterojunctions under visible light irradiation. This work opens up new prospects for constructing other perovskite-based nanosheets photocatalysts or designing other 2D-2D heterojunction photocatalysts for the photocatalytic degradation of organic pollutant.

References

[1] T. Shibata, G. Takanashi, T. Nakamura, K. Fukuda, Y. Ebina, T. Sasaki, Energy Environ. Sci. 4 (2011) 535–542.
[2] S.J.A. Moniz, S.A. Shevlin, D.J. Martin, Z.X. Guo, J.W. Tang, Energy Environ. Sci. 8 (2015) 731–759.
[3] J.G. Tao, T. Luttrell, M. Batzill, Nat. Chem. 3 (2011) 296–300.
[4] M. Osada, T. Sasaki, Adv. Mater. 24 (2012) 210–228.
[5] K.J. Koski, Y. Cui, ACS Nano 7 (2013) 3739–3743.
[6] K.S. Novoselov, D. Jiang, F. Schedin, T.J. Booth, V.V. Khotkevich, S.V. Morozov, A.K. Geim, Proc. Natl. Acad. Sci. U. S. A. 102 (2005) 10451–10453.
[7] Y. Hou, Z.H. Wen, S.M. Cui, X.R. Guo, J.H. Chen, Adv. Mater. 25 (2013) 6291–6297.
[8] K.S. Virdi, Y. Kauffmann, C. Ziegler, P. Ganter, P. Blaha, B.V. Lotsch, W.D. Kaplan, C. Scheu, J. Phys. Chem. C 120 (2016) 11170–11179.
[9] Y. Ebina, T. Sasaki, M. Harada, M. Watanabe, Chem. Mater. 14 (2002) 4390–4395.
[10] Y. Ebina, K. Akatsuka, K. Fukuda, T. Sasaki, Chem. Mater. 24 (2012) 4201–4208.
[11] Y. Ebina, N. Sakai, T. Sasaki, J. Phys. Chem. B 109 (2005) 17212–17216.
[12] T.W. Kim, S.G. Hur, S.J. Hwang, H. Park, W. Choi, J.H. Choy, Adv. Funct. Mater. 17 (2007) 307–314.
[13] J.L. Gunjakar, T.W. Kim, H.N. Kim, I.Y. Kim, S.J. Hwang, J. Am. Chem. Soc. 133 (2011) 14998–15007.
[14] H.Y. Yuan, M. Nguyen, T. Hammer, G. Koster, G. Rijnders, J.E. Elshof, ACS Appl. Mater. Interfaces 7 (2015) 27473–27478.
[15] Y. Okamoto, S. Ida, J. Hyodo, H. Hagiwara, T. Ishihara, J. Am. Chem. Soc. 133 (2011) 18034–18037.
[16] N. Toihara, Y. Yoneyama, A. Shimada, S. Taharab, Y. Sugahara, Dalton Trans. 44 (2015) 3002–3008.
[17] T. Oshima, M. Eguchi, K. Maeda, ChemSusChem 9 (2016) 396–402.
[18] Y.J. Song, N. Iyi, T. Hoshide, T.C. Ozawa, Y. Ebina, R.Z. Ma, N. Miyamoto, T. Sasaki, Chem. Commun. 51 (2015) 17068–17071.
[19] O.C. Compton, E.C. Carroll, J.Y. Kim, D.S. Larsen, F.E. Osterloh, J. Phys. Chem. C 111 (2007) 14589–14592.
[20] E.M. Sabio, R.L. Chamousis, N.D. Browning, F.E. Osterloh, J. Phys. Chem. C 116 (2012) 3161–3170.
[21] M. Osada, G. Takanashi, B.W. Li, K. Akatsuka, Y. Ebina, K. Ono, H. Funakubo, K. Takada, T. Sasaki, Adv. Funct. Mater. 21 (2011) 3482–3487.
[22] E.M. Sabio, M.F. Chi, N.D. Browning, F.E. Osterloh, Langmuir 26 (2010) 7254–7261.
[23] E.C. Carroll, O.C. Compton, D. Madsen, F.E. Osterloh, D.S. Larsen, J. Phys. Chem. C 112 (2008) 2395–2403.
[24] K. Maeda, M. Eguchi, T. Oshima, Angew. Chem. 53 (2014) 13164–13168.
[25] Y.S. Han, I. Park, J.H. Choy, J. Mater. Chem. 11 (2001) 1277–1282.
[26] D.B. Xu, S.B. Yang, Y. Jin, M. Chen, W.Q. Fan, B.F. Luo, W.D. Shi, Langmuir 31 (2015) 9694–9699.
[27] K. Maeda, G. Sahara, M. Eguchi, O. Ishitani, ACS Catal. 5 (2015) 1700–1707.
[28] T. Oshima, D.L. Lu, O. Ishitani, K. Maeda, Angew. Chem. 54 (2015) 2698–2702.
[29] T. Oshima, D.L. Lu, K. Maeda, ChemNanoMat (2016) 201600072, http://dx.doi.org/10.1002/cnma.
[30] L. Li, R.Z. Ma, Y. Ebina, K. Fukuda, K. Takada, T. Sasaki, J. Am. Chem. Soc. 129 (2007) 8000–8007.
[31] Y.H. Ao, K.D. Wang, P.F. Wang, C. Wang, J. Hou, Appl. Catal. B: Environ. 194 (2016) 157–168.
[32] F. Dong, T. Xiong, Y.J. Sun, Y.X. Zhang, Y. Zhou, Chem. Commun. 51 (2015) 8249–8252.
[33] Y.H. Ao, K.D. Wang, P.F. Wang, C. Wang, J. Hou, Dalton Trans. 45 (2016) 7986–7997.
[34] C.X. Wang, M. Osada, Y. Ebina, B.W. Li, K. Akatsuka, K. Fukuda, W. Sugimoto, R.Z. Ma, T. Sasaki, ACS Nano 8 (2014) 2658–2666.
[35] B. Bajorowicz, J. Reszczyńska, W. Lisowski, T. Klimczuk, M. Winiarski, M. Słomade, A.Z. Medynska, RSC Adv. 5 (2015) 91315–91325.
[36] X.C. Wang, K. Maeda, A. Thomas, K. Takanabe, G. Xin, J.M. Carlsson, K. Domen, M. Antonietti, Nat. Mater. 8 (2009) 76–80.
[37] J. Xu, K. Shen, B. Xue, Y.X. Li, Y. Cao, Catal. Lett. 143 (2013) 600–609.
[38] S.C. Yan, Z.S. Li, Z.G. Zou, Langmuir 25 (2009) 10397–10401.
[39] Y. Zheng, L.H. Lin, X.J. Ye, F.S. Guo, X.C. Wang, Angew. Chem. 53 (2014) 11926–11930.
[40] Y.M. He, L.H. Zhang, M.H. Fan, X.X. Wang, M.L. Walbridge, Q.Y. Nong, Y. Wu, L.H. Zhao, Solar Energy Mater. Solar Cells 137 (2015) 175–184.
[41] T.T. Li, L.H. Zhao, Y.M. He, J. Cai, M.F. Luo, J.J. Lin, Appl. Catal. B: Environ. 129 (2013) 255–263.
[42] L.Q. Shao, D.L. Jiang, P. Xiao, L.M. Zhu, S.C. Meng, M. Chen, Appl. Catal. B: Environ. 198 (2016) 200–210.

[43] J. Fu, B.B. Chang, Y.L. Tian, F.N. Xia, X.P. Dong, J. Mater. Chem. A 1 (2013) 3083–3090.
[44] Y.Z. Hong, Y.H. Jiang, C.S. Li, W.Q. Fan, X. Yan, M. Yan, W.D. Shi, Appl. Catal. B: Environ. 180 (2016) 663–673.
[45] L. Ge, C.C. Han, J. Liu, Appl. Catal. B: Environ. 108–109 (2011) 100–107.
[46] Y.M. He, Y. Wang, L.H. Zhang, B.T. Teng, M.H. Fan, Appl. Catal. B: Environ. 168–169 (2015) 1–8.
[47] K. Sridharan, E. Jang, T.J. Park, Appl. Catal. B: Environ. 142–143 (2013) 718–728.
[48] W. Liu, M.L. Wang, C.X. Xu, S.F. Chen, X.L. Fu, J. Mol. Catal. A: Chem. 368 (2013) 9–15.
[49] C.S. Pan, J. Xu, Y.J. Wang, D. Li, Y.F. Zhu, Adv. Funct. Mater. 22 (2012) 1518–1524.
[50] F.F. Shi, L.L. Chen, C.S. Xing, D.L. Jiang, D. Li, Min Chen, RSC Adv. 4 (2014) 62223–62229.
[51] X. Xu, G. Liu, C. Randorn, J.T.S. Irvine, Int. J. Hydrogen Energy 36 (2011) 13501–13507.
[52] D.M. Chen, K.W. Wang, D.G. Xiang, R.L. Zong, W.Q. Yao, Y.F. Zhu, Appl. Catal. B: Environ. 147 (2014) 554–561.
[53] M.M. Fang, C.H. Kim, T.E. Mallouk, Chem. Mater. 11 (1999) 1519–1525.
[54] D.L. Jiang, J. Li, C.S. Xing, Z.Y. Zhang, S.C. Meng, M. Chen, ACS Appl. Mater. Interfaces 7 (2015) 19234–19242.
[55] H. Hata, Y. Kobayashi, V. Bojan, W.J. Youngblood, T.E. Mallouk, Nano Lett. 8 (2008) 794–799.
[56] H. Suzuki, O. Tomita, M. Higashi, R. Abe, Catal. Sci. Technol. 5 (2015) 2640–2648.
[57] D.L. Jiang, J.J. Zhu, M. Chen, J.M. Xie, J. Colloid Interface Sci. 417 (2014) 115–120.
[58] J.J. Ma, Z.Y. Zhang, M. Yang, Y.J. Wu, X.C. Feng, L. Liu, X.B. Zhang, Z.W. Tong, Microporous Mesoporous Mater. 221 (2016) 123–127.
[59] T.Y. Ma, Y.H. Tang, S. Dai, S.Z. Qiao, Small 10 (2014) 2382–2389.
[60] C.Y. Liu, Y.H. Zhang, F. Dong, X. Du, H.W. Huang, J. Phys. Chem. C 120 (2016) 10381–10389.
[61] K.X. Li, Z.X. Zeng, L.S. Yan, S.L. Luo, X.B. Luo, M.X. Huo, Y.H. Guo, Appl. Catal. B: Environ. 165 (2015) 428–437.
[62] Y.J. Wang, R. Shi, J. Lin, Y.F. Zhu, Energy Environ. Sci. 4 (2011) 2922–2929.
[63] J.J. Ding, B. Hong, Z.L. Luo, S. Sun, J. Bao, C. Gao, J. Phys. Chem. C 118 (2014) 27690–27697.
[64] Z.Y. Zhang, D.L. Jiang, D. Li, M.Q. He, M. Chen, Appl. Catal. B: Environ. 183 (2016) 113–123.
[65] B. Chai, T.Y. Peng, J. Mao, K. Li, L. Zan, Phys. Chem. Chem. Phys. 14 (2012) 16745–16752.
[66] Q. Zhang, D.Q. Lima, I. Lee, F. Zaera, M.F. Chi, Y.D. Yin, Angew. Chem. 123 (2011) 7226–7230.
[67] T.C. Ozawa, M. Onoda, N. Iyi, Y. Ebina, T. Sasaki, J. Phys. Chem. C 118 (2014) 1729–1738.
[68] Z.F. Jiang, D.L. Jiang, Z.X. Yan, D. Liu, K. Qian, J.M. Xie, Appl. Catal. B: Environ. 170–171 (2015) 195–205.
[69] T.Y. Wang, W. Quan, D.L. Jiang, L.L. Chen, D. Li, S.C. Meng, M. Chen, Chem. Eng. J. 300 (2016) 280–290.
[70] X.D. Zhu, Y.J. Wang, R.J. Sun, D.M. Zhu, Chemosphere 92 (2013) 925–932.
[71] P. Mahamallik, S. Saha, A. Pal, Chem. Eng. J. 276 (2015) 155–165.
[72] X.L. Liu, P. Lv, G.X. Yao, C.C. Ma, P.W. Huo, Y.S. Yan, Chem. Eng. J. 217 (2013) 398–406.
[73] J.F. Niu, S.Y. Ding, L.W. Zhang, J.B. Zhao, C.H. Feng, Chemosphere 93 (2013) 1–8.
[74] P.T. Xu, T.J. Milstein, T.E. Mallouk, ACS Appl. Mater. Interfaces 8 (2016) 11539–11547.
[75] D.L. Jiang, L.L. Chen, J.J. Zhu, M. Chen, W.D. Shi, J.M. Xie, Dalton Trans. 42 (2013) 15726–15734.
[76] J.G. Yu, L.F. Qi, M. Jaroniec, J. Phys. Chem. C 114 (2010) 13118–13125.
[77] H. Li, J. Liu, W. Hou, N. Du, R. Zhang, X. Tao, Appl. Catal. B: Environ. 89 (2014) 160–161.
[78] Y.J. Yuan, D.Q. Chen, Y.W. Huang, Z.T. Yu, J.S. Zhong, T.T. Chen, W.G. Tu, Z.J. Guan, D.P. Cao, Z.G. Zou, ChemSusChem 9 (2016) 1003–1009.
[79] J.H. Xu, W.Z. Wang, S.M. Sun, L. Wang, Appl. Catal. B: Environ. 111–112 (2012) 126–132.
[80] Y.M. He, L.H. Zhang, B.T. Teng, M.H. Fan, Environ. Sci. Technol. 49 (2015) 649–656.
[81] Z.F. Jiang, C.Z. Zhu, W.M. Wan, K. Qian, J.M. Xie, J. Mater. Chem. A 4 (2016) 1806–1818.
[82] M. Xu, W.D. Zhang, Eur. J. Inorg. Chem. 6 (2016) 826–831.
[83] C.S. Pan, T. Takata, K. Kumamoto, S.S.K. Ma, K. Ueda, T. Minegishi, M. Nakabayashi, T. Matsumoto, N. Shibata, Y. Ikuharad, K. Domen, J. Mater. Chem A. 4 (2016) 4544–4552.